ACS APPLIED MATERIALS & INTERFACES

Research Article

www.acsami.org

Bifunctional-Nanotemplate Assisted Synthesis of Nanoporous $SrTiO_3$ Photocatalysts Toward Efficient Degradation of Organic Pollutant

Shuxin Ouyang,*[,†,‡,⊥] Peng Li,[§,⊥] Hua Xu,[†,‡] Hua Tong,[†,‡] Lequan Liu,[§] and Jinhua Ye*[,†,‡,§]

[†]TU-NIMS Joint Research Center and Tianjin Key Laboratory of Composite and Functional Materials, School of Material Science and Engineering, Tianjin University, Tianjin 300072, People's Republic of China

[‡]Collaborative Innovation Center of Chemical Science and Engineering (Tianjin), Tianjin 300072, People's Republic of China

[§]International Center for Materials Nanoarchitectonics (WPI-MANA) and Environmental Remediation Materials Unit, National Institute for Materials Science (NIMS), Tsukuba 305-0047, Japan

Supporting Information

ABSTRACT: Nanoporous $SrTiO_3$ photocatalysts were fabricated via a novel technique, the nanotemplate assisted sol–gel hydrothermal reaction. In the alkaline-environment hydrothermal reaction, the SiO_2 nanotemplate not only served as pore generator but also worked on adjusting the local reaction environment around the $SrTiO_3$ nanocrystals. This contributed to a continuous modulation between the surface area and the crystallinity of the photocatalyst. The photocatalytic activities of the nanoporous $SrTiO_3$ samples were evaluated by the degradation of gaseous isopropyl alcohol (IPA). Due to an optimal equilibrium between surface area and crystallinity, a $SrTiO_3$ sample synthesized via adding 40% template (STO-SiO_2-40%) showed the highest activity, which achieves 40 and 8 times of enhancement of CO_2 evolution in comparison with the sample prepared without template and a commercial nano-$SrTiO_3$, respectively. The photodegradation mechanism of IPA over this sample was also investigated in detail. This synthetic technique is also available to prepare the other nanoporous titanates, such as doped $SrTiO_3$ samples and alkali-metal titanates.

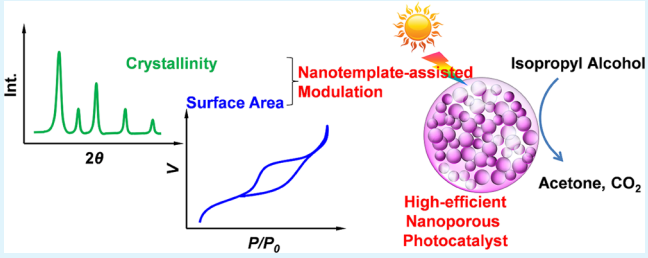

KEYWORDS: *nanoporous material, nanotemplate, photocatalysis, surface area, crystallinity, organic pollutant photodegradation*

INTRODUCTION

Semiconductor photocatalysis driven contaminant elimination, hydrogen production, and CO_2 reduction is a potential and promising technology for humans' sustainable development based on solar energy.[1−6] Besides traditional TiO_2, ZnO, and their modified materials,[7−11] most of the newly developed photocatalysts are multimetal oxides, such as Ag-based, Bi-based, Ti-based, and Ta-based materials,[12−18] because the multimetal components offer a wider choice for further modifications on the basis of energy-band and surface-chemistry engineerings to enhance the photocatalytic efficiency. It is well-known that the surface area of a catalyst greatly affects its catalytic efficiency.[19] Thus, fabricating porous-structured multimetal oxides with high surface areas has drawn extensive attention.[20−24]

However, the surface areas of multimetal-oxide photocatalysts synthesized by present techniques are mostly limited at around 100 m^2/g.[20,22−24] Furthermore, most of the successful examples are based on the evaporation-induced self-assembly (EISA) method, which usually needs a further sintering at 350−550 °C for several hours to remove organic compositions.[20−22] Recently, we have developed a low-temperature ion-exchange route to prepare porous Ga- and Ge-based photocatalysts, but nevertheless, the $NaGaO_2$ and Na_2GeO_3 precursors were obtained by a solid-state reaction at 850−900 °C.[23,24] Thereby, a low-temperature synthetic technique to fabricate porous multimetal-oxide photocatalysts is still a big challenge. Besides the surface area, the crystallinity is another important factor for photocatalyst, because the poor crystallinity terribly increases the recombination of electrons and holes and thus suppresses the photocatalytic efficiency;[25,26] however, most of the newly exploited synthetic methods have ignored this issue.

The titanates, such as $SrTiO_3$,[27−29] alkali-metal titanates,[30−32] and their doped materials,[28,33,34] are a class of photocatalysts that are well-known for their high efficiency, durable stability, and low cost. The facile hydrothermal reaction has been widely adopted to prepare these titanates,[28,35,36] and the alkaline concentration of reaction environment plays a significant role on the crystallinity of product.[37,38] The hard-template assisted synthesis is also a conventional approach to fabricate porous material and the template removal requires a post-treatment of alkaline-solution cleaning or calcination.[39,40] If the hard template is introduced into the alkaline-environment

Received: October 7, 2014
Accepted: November 21, 2014
Published: November 21, 2014

hydrothermal reaction to produce the above-mention titanates, the hard template could be corroded in the alkaline environment and then the porous structure will be generated; meanwhile, the alkaline concentration in synthesis will be changed because of the retroaction of hard-template removal, which will affect the crystallinity. This strategy will achieve a bifunctional application of the template in synthesis. Herein, we designed the conversion of SiO_2 nanotemplate to Na_2SiO_3 into the hydrothermal reaction for synthesizing $SrTiO_3$ photocatalyst (detailed synthesis and characterizations are introduced in the Experimental Methods and Supporting Information, SI-1). At a synthesis temperature as low as 150 °C, the surface areas of the $SrTiO_3$ samples could be enlarged from 17 to 432 m^2/g and, meanwhile, the crystallinity could be significantly reduced; this continuous modulation between surface area and crystallinity contributes to a significant enhancement of photocatalytic activity of isopropyl alcohol (IPA) degradation over $SrTiO_3$. Furthermore, the universality of this synthetic method was verified via preparing the other nanoporous titanates, such as doped $SrTiO_3$ samples and alkali-metal titanates (as reported in Tables S1, SI-8, and SI-9 in the Supporting Information).

RESULTS AND DISCUSSION

The adopted SiO_2 nanotemplate is a commercially available and very cheap chemical (No.192-09071, Wako, Japan; details of this material are shown in the Supporting Information, SI-2). It is an amorphous phase and consists of irregular fine particles with an average size of 10−20 nm (Supporting Information, Figure S2a,b). It possesses good dispersion and a large surface area of 389 m^2/g (Supporting Information, Figure S2b,c,d).

Under the SiO_2 nanotemplate assistant, the nanoporous structure is facile to be generated in the $SrTiO_3$ photocatalyst. Taking the STO-SiO_2-40% as an example, as exhibited in Figure 1a, the typical Type-IV isotherm and its hysteresis loop indicates that the sample contains a porous structure. The half pore width (HPW) of major pores is smaller than 5 nm and a small amount of micropore is also observed (HPW < 1 nm). From transmission electron microscopy (TEM) images (Figure 1b,c), the average size of particles is estimated to be around 200 nm and the porous structure can be clearly observed. The high-resolution transmission electron microscopy (HRTEM) image of a typical particle edge (Figure 1c, inset) presents two-dimension crystal lattice stripes with lattice spacing of 2.758 Å and a 60° interfacial angle, which corresponds to (101) and (110) crystal planes of $SrTiO_3$. The above-mentioned results indicate the sample is crystallized $SrTiO_3$ with a nanoporous structure.

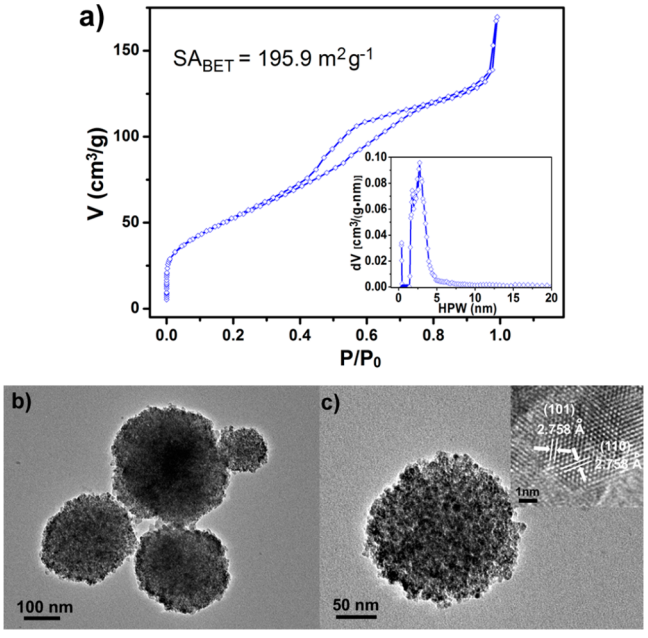

Figure 1. Microstructure characterizations of STO-SiO_2-40% sample. (a) Nitrogen adsorption−desorption isotherms and pore distribution analyzed by DFT (density functional theory) simulation (inset); HPW, half pore width. (b,c) TEM and HRTEM (c, inset) images.

The template-amount-dependent morphology, pore-feature, and chemical composition variations were further systematically studied. According to observation from TEM images (Figure 2), the particle sizes of as-prepared $SrTiO_3$ samples obviously decrease when the nanotemplate amount exceeds 50% (Figure 2a−e). The shapes of particles change from cube-like to spherical and then to sphere-like figures when the nanotemplate amount increases from 0% to 30%, but it is difficult to keep the sphere-like shape as the nanotemplate amount exceeds 50% because of the loose structure (Figure 2f−j). When the nanotemplate amount increases to 70%, poor crystallinity results in that the crystal lattice stripe is difficult to be observed. The pore distributions analyzed via DFT (density functional

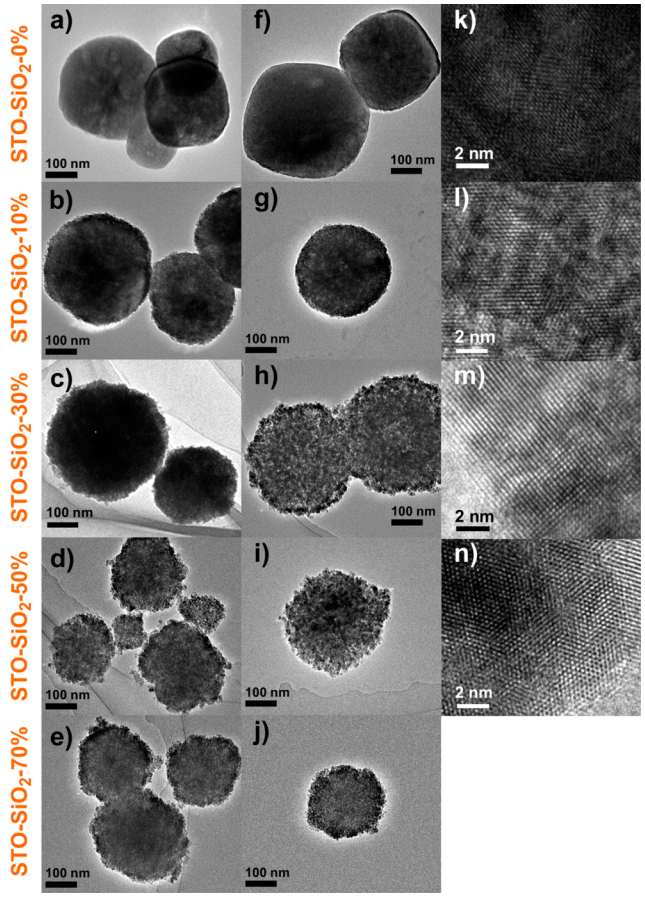

Figure 2. TEM and HRTEM images of STO-SiO_2-0%, STO-SiO_2-10%, STO-SiO_2-30%, STO-SiO_2-50%, and STO-SiO_2-70% samples. (a−e) TEM images; (f−j) TEM images to show pore structures; (k−n) HRTEM images.

dx.doi.org/10.1021/am506877b | ACS Appl. Mater. Interfaces 2014, 6, 22726−22732

theory) and HK (Horvath−Kawazoe) simulations reveal the change of pore features (Figure 3). Both the micropore and

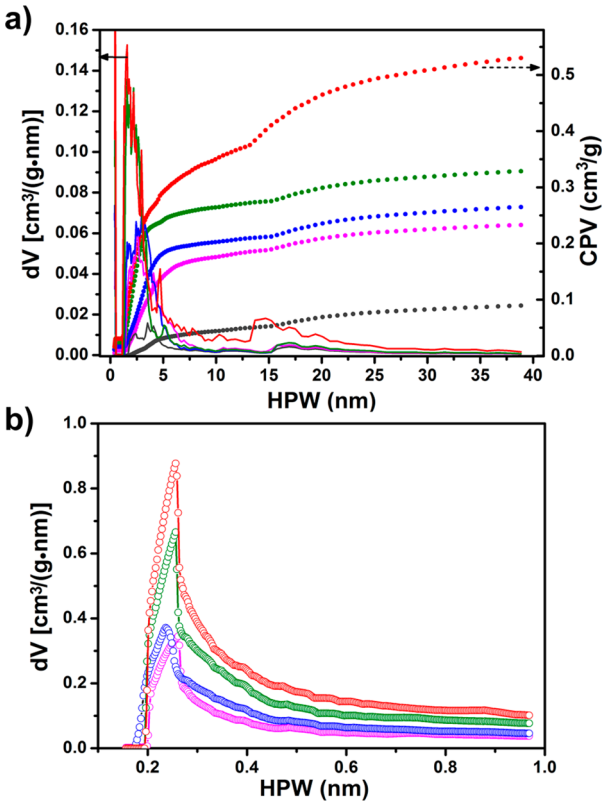

Figure 3. (a) Pore distribution and cumulative pore volume analyzed by DFT (density functional theory) simulation. (b) Micropore distribution analyzed by HK (Horvath−Kawazoe) simulation; HPW, half pore width; CPV, cumulative pore volume. STO-SiO_2-90%, red curves; STO-SiO_2-70%, dark green curves; STO-SiO_2-50%, blue curves; STO-SiO_2-30%, magenta curves; STO-SiO_2-10%, dark gray curves.

mesopore volumes increase with adding more nanotemplate. We calculated the pore distribution percentages for as-prepared $SrTiO_3$ samples, which indicate that the relatively uniform pore distribution (the percentage of 1 nm < HPW < 10 nm exceeds 70%) is easy to be attained when the used nanotemplate amount is between 30% and 80% (Supporting Information, SI-3, Table S2). The chemical compositions of nanoporous $SrTiO_3$ samples were measured via inductively coupled plasma optical emission spectroscopy (ICP-OES). The ratios of Sr to Ti closely equal to 1.0 to 1.0 with a 0.7% maximum deviation; the Si impurity gradually increases with adding more nanotemplate (Supporting Information, SI-3, Table S3).

Interestingly, the amount of SiO_2 nanotemplate not only influences the surface area but also affects the crystallinity of as-prepared samples, although the synthetic conditions (hydrothermal temperature and alkaline concentration) were kept the same. As presented in Figure 4, the X-ray diffraction (XRD) patterns of the $SrTiO_3$ samples indicate that they crystallize in a typical perovskite structure of the cubic symmetry; with increasing the SiO_2 template amount, the crystallinities of samples decrease. We introduce the full width at half-maximum (FWHM) of the XRD pattern as a semiquantitative index of the crystallinity; a small value of FWHM implies a high crystallinity of sample. The strongest peak corresponding to (110) crystal

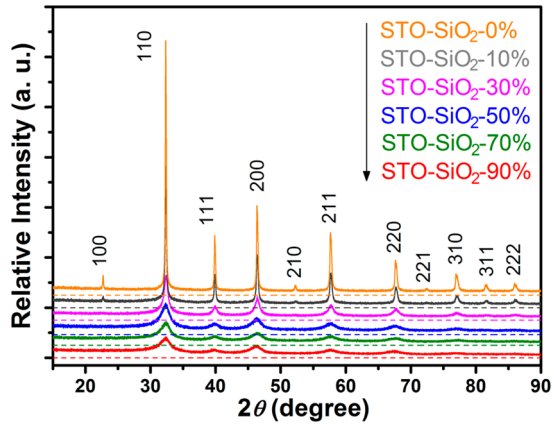

Figure 4. Template-amount-dependent variations of XRD patterns of as-prepared $SrTiO_3$ samples; dash lines are the baselines of each samples, where absolute intensities = 0.

plane was used to calculate the FWHM (see the detailed calculation method in the Supporting Information, SI-4). As the nanotemplate amount increases, the values of FWHM gradually increase from 0.18 to 1.84° (Table 1), indicating a significant reduction of the crystallinity.

How does the SiO_2 nanotemplate affect the crystallinity of $SrTiO_3$ sample in synthesis? A contrast study of the reaction-time-dependent crystallinity variation between the STO-SiO_2-0% and STO-SiO_2-90% samples was carried out (Supporting Information, SI-5, Figure S4 and Table S4). Furthermore, the reaction-time-dependent conversion of SiO_2 to Na_2SiO_3 in the synthesis of STO-SiO_2-90% sample was studied via ICP-OES measurement (Supporting Information, SI-5, Table S5). It was found that the slow release of Na_2SiO_3 derived from SiO_2 influenced the local reaction environment and subsequently controlled the crystal growing condition, which finally affected the crystallinity.

Based on the above analysis, the formation mechanism of $SrTiO_3$ with controllable surface area and crystallinity via bifunctional-nanotemplate assisted sol−gel hydrothermal technique is proposed, as depicted in Scheme 1. The $SiO_2/SrTiO_3$ precursor goes through a state of suspension (Scheme 1a) to a form of gel under drying treatment (Scheme 1b). During alkaline-environment hydrothermal reaction, the SiO_2 nanotemplates inserted in the surface and inner of $SrTiO_3$ particle are corroded and dissolved by NaOH solution to generate porous structure, $SiO_2 + NaOH \rightarrow Na_2SiO_3 + H_2O$ (Scheme 1c(i)); however, the desorption and dispersion of Na_2SiO_3 products undergo a very slow process, lending to an interlayer (includes SiO_2, Na_2SiO_3, and NaOH) leaving between the surface of $SrTiO_3$ crystal and the NaOH aqueous solution (Scheme 1c(ii)). This interlayer possesses relatively lower alkaline concentration than the outer NaOH solution, which can control the crystallization moderately. Therefore, the amount of SiO_2 nanotemplate determines the generated pore volume and meanwhile the interlayer composition, namely local reaction environment, which modulates both the surface area and the crystallinity of as-prepared sample.

Next, the IPA photodegradation was adopted to verify the validity of continuous adjustment between the crystallinity and the surface area over the $SrTiO_3$ photocatalyst. The IPA photodegradation is a classical model reaction. The photo-oxidization of IPA to acetone is a one-electron process; after that, the acetone could be further oxidized into CO_2 through a

Table 1. Crystallinities, Surface Areas, and Photocatalytic Activities of $SrTiO_3$ Samples

STO-SiO_2-x%	0%	10%	30%	40%	50%	70%	90%	C-Nano-STO
surface area, $m^2\ g^{-1}$	17.1	30.3	159.3	195.9	212.0	325.6	431.6	20.1
crystallinity, FWHM, deg	0.18	0.23	0.72	1.07	1.53	1.68	1.84	0.18
R(acetone) in IPA P.D.[a]	1.9	5.3	65.9	72.5	48.7	18.5	5.3	15.1
$R(CO_2)$ in IPA P.D.[b]	0.13	0.35	4.90	5.39	3.58	1.95	0.32	0.57

[a]Acetone evolution rate in IPA photodegradation, μmol h^{-1}. [b]CO_2 evolution rate in IPA photodegradation, μmol h^{-1}.

Scheme 1. Formation Mechanism of Porous $SrTiO_3$ with Bifunctional SiO_2 Nanotemplate[a]

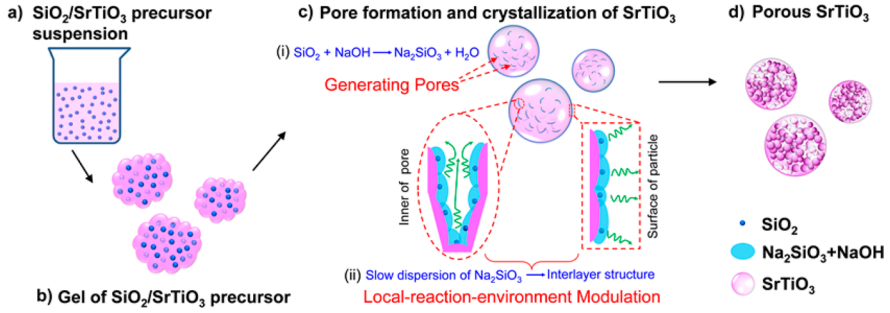

[a](a) Preparing $SiO_2/SrTiO_3$ precursor suspension; (b) generating gel of $SiO_2/SrTiO_3$ precursor; (c) pore formation and crystallization of $SrTiO_3$; (d) final product of porous $SrTiO_3$.

multielectron oxidization process. The variation tendencies of acetone and CO_2 evolution rates (during first 60 min) over as-prepared $SrTiO_3$ samples keep the same, as presented in Figure 5a. When the template amount is lower than 40%, the increase of surface areas dominates the enhancement of photoactivity; as the template amount is higher than 40%, the decrease of crystallinities suppresses the photoactivity. Because of optimization between surface area and crystallinity, the STO-SiO_2-40% attains the highest photocatalytic activity among these $SrTiO_3$ samples (Figure 5a and Table 1). The acetone/CO_2 evolution rate over this sample achieves 37/40 and 13/16 times of enhancement in comparison with the STO-SiO_2-0% and STO-SiO_2-90%, respectively. As aforementioned about the chemical compositions of the nanoporous $SrTiO_3$ samples, the Si impurity gradually increases with adding more nanotemplate (Supporting Information, SI-3, Table S3). The SiO_2 template residual could enrich reactant around the surface of photocatalyst, which will probably enhance the photoactivity. However, the change tendency of photocatalytic efficiency over the $SrTiO_3$ samples did not follow a continuous enhancement with the template residual increasing. Therefore, the overall effect of surface area and crystallinity but not the influence of SiO_2 template residual is the main reason to result in the present variation tendency of photoactivity. Additionally, the photocatalytic activity of the STO-SiO_2-40% was compared with a commercial Nano-$SrTiO_3$ (C-Nano-STO, detailed characterizations of this material are listed in the Supporting Information, SI-6). The former achieves a 3.8 and 8.4 times enhancement for acetone and CO_2 evolution rates, respectively (as shown in Figure 5b). Therefore, it can be seen that this strategy of continuous optimization between the surface area and the crystallinity over photocatalyst is highly effectual.

A long-term experiment over STO-SiO_2-40% was carried out to study the IPA photodegradation process (as shown in Figure 6). At the initial stage (irradiation time = 0–20 min), most of the IPA molecules were photo-oxidized into acetone accompanied with partially completed degradation to CO_2. After all the IPA was photo-oxidized into acetone (irradiation

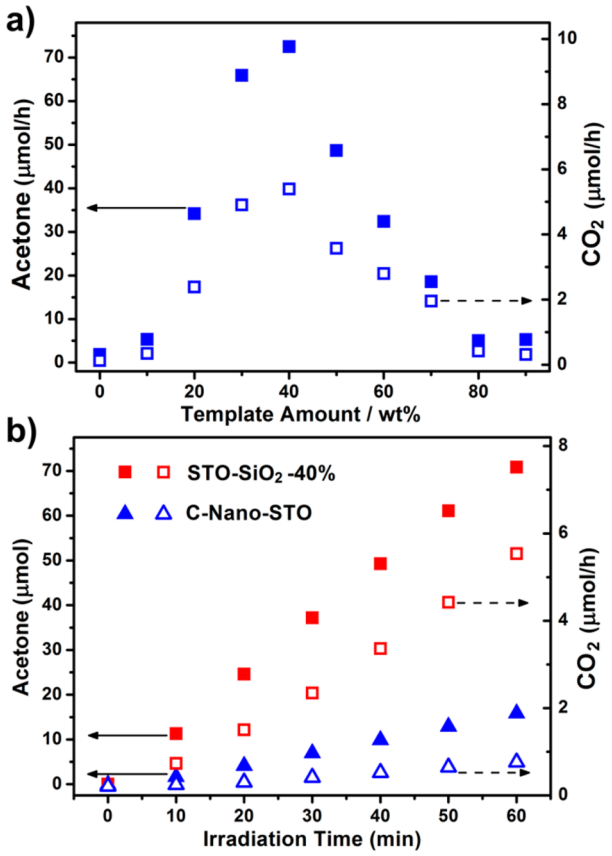

Figure 5. (a) Acetone (■) and CO_2 (□) evolution rates of IPA photodegradation over the $SrTiO_3$ samples with different amounts of SiO_2 as template. (b) Acetone and CO_2 evolution amounts of IPA photodegradation over STO-SiO_2-40% and commercial available nano-$SrTiO_3$ samples under UV–visible light irradiation as a function of irradiation time. Catalyst, 100 mg; light source, full-arc Xe lamp (λ > 300 nm, light intensity = 66.9 mW/cm^2).

dx.doi.org/10.1021/am506877b | ACS Appl. Mater. Interfaces 2014, 6, 22726–22732

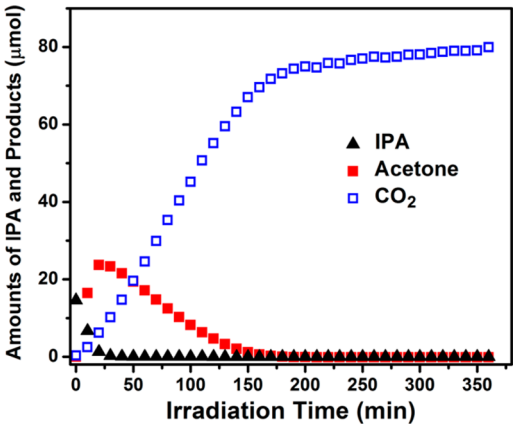

Figure 6. Long-term experiment of IPA photodegradation over STO-SiO_2-40%. Catalyst, 50 mg; light source, full-arc Xe lamp (λ > 300 nm, light intensity = 66.9 mW/cm^2).

time = around 30 min), the acetone degradation began to dominate in the photocatalytic reaction; it could be found the gradual acetone elimination and the continuous CO_2 evolution. This period lasted for long time until the acetone in the gas phase completely disappeared (irradiation time = around 180 min). To explore the stability of photoactivity, the cycle experiment with an irradiation period of 180 min was performed (see the Supporting Information, SI-7). For all three cycles, the IPA was totally degraded in 30 min and the acetone was completely removed in 180 min. Because of a little difference of initial IPA concentration, the evolution amounts of CO_2 in the three cycles showed slight disparity. These results indicate that the photoactivity of the as-prepared nanoporous $SrTiO_3$ is relatively stable.

The reactive species in the photodegradation process is one of the most concerning issues for researchers. However, most of the previous studies on the reactive species were focused on the photodegradation in the aqueous-solution phase;[41−44] few works have reported the results about the reactive species in the gas-phase photodegradation. Herein, we studied the active species of $SrTiO_3$ for the gaseous IPA photodegradation via a method of introducing scavengers. The ·OH, h^+, and $\cdot O_2^-$ are the main reactive species in the IPA photodegradation.[45,46] The *t*-butyl alcohol (tBA), ammonium oxalate (AO), and *p*-benzoquinone (pBQ) were adopted and served as the scavengers for ·OH, h^+, and $\cdot O_2^-$, respectively. The AO and pBQ were coated on the surface of sample with a mass percentage of 5% and the tBA were mixed into IPA gas with a volume percentage of 5%. To avoid the mineralization of the scavengers to release CO_2 that interfered in the measurements for IPA photodegradation, the light intensity of the studies on reactive species was decreased. As exhibited in Figure 7a, after introducing tBA, AO, and pBQ, the photoactivity for oxidizing IPA to acetone reduced by about 46%, 41%, and 87%, respectively, indicating that all of the active species, ·OH, h^+, and $\cdot O_2^-$, participated in the initial oxidization of IPA (IPA to acetone) but the $\cdot O_2^-$ dominated this reaction. On the other hand, as presented in Figure 7b, the introduced AO and tBA could obviously reduce the photoactivity of completed mineralization of IPA (IPA to CO_2) while the influence of pBQ was negligible, which implies that the completed photodegradation of IPA was induced by h^+ and its derivate active species ·OH.

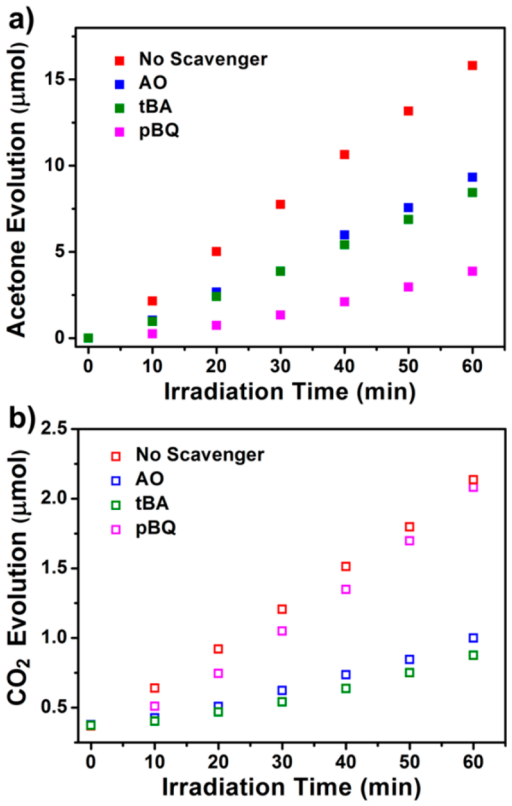

Figure 7. IPA photodegradations over STO-SiO_2-40% with different reactive-species scavengers. (a) Acetone evolution amounts; (b) CO_2 evolution amounts. Catalyst, 50 mg; light source, full-arc Xe lamp (λ > 300 nm, light intensity = 7.4 mW/cm^2).

More importantly, this nanotemplate assisted sol−gel hydrothermal technique is proved to be a relatively universal approach. The synthetic technique introduced herein is available to fabricate the nanoporous doped $SrTiO_3$ materials, such as Cr doped $SrTiO_3$ and La, Cr codoped $SrTiO_3$ (Supporting Information, SI-1, SI-8). It also succeeds in synthesizing the porous alkali-metal titanates, such as Li_2TiO_3, $Na_2Ti_3O_7$, and $K_2Ti_4O_9$ (Supporting Information, SI-1, SI-9). Furthermore, it is also expected to be applicable for a series of alkali-metal and alkali-earth-metal niobates, tantalates, and their modified forms as doping and solid solution, which are worthy to be further attempted.

CONCLUSIONS

In conclusion, a relatively universal route to fabricate nanoporous titanates, the nanotemplate assisted sol−gel hydrothermal technique, is developed in this study. The nanotemplate plays bifunctional roles in generating pores and controlling the local reaction environment. Thus, as exemplified by the $SrTiO_3$, the present synthetic process continuously optimizes the balance between the surface area and the crystallinity of this material, which helps to attain a great enhancement of its photocatalytic efficiency for eliminating gaseous IPA. This study reveals that the advanced synthetic technique which involves the nanotemplate and the interface chemistry supplies maturing skill for optimizing photocatalyst, which therefore remarkably improves photocatalytic performance.

EXPERIMENTAL METHODS

Sample Synthesis. In a typical procedure, about 5 mmol titanium tetra-*n*-butoxide and 5 mmol strontium acetate hemihydrate served as precursors and were dissolved in ethanol and glacial acetic acid, respectively. Then, these two solutions were mixed with each other slowly. After that, a certain amount of SiO_2 nanotemplate was added into the mixed solution, and then the solution was ultrasonically treated for 1 h to make SiO_2 nanotemplate disperse uniformly. Followed with a sol−gel hydrothermal procedure as shown in the flowchart (Supporting Information, SI-1, Figure S1), the porous $SrTiO_3$ could be generated. The products usually contained some $SrCO_3$ impurity. It could be removed by dispersing the sample into an extremely dilute acetic acid solution and stirring for 5 h; in the whole process, the pH value was kept at 4−6 by dripping into acetic acid. After that, the sample was cleaned by ultrapure water and centrifugally separated until the solution pH value became 7. After the material was dried at 70 °C overnight, the final product was obtained. The samples were entitled as STO-SiO_2-*x*%, in which *x*% indicates the mass percentage of the SiO_2 nanotemplate to the theoretical yield of STO product. This synthetic technique is also available for the doped $SrTiO_3$ and other alkali-metal titanates. The details of synthesis are introduced in the Supporting Information, SI-1, Table S1.

Characterization. Crystal structures of the samples were determined using powder X-ray diffraction (X'Pert Pro; PANalytical Corp.) with Cu Kα_1 radiation. Chemical compositions of the samples were analyzed by inductively coupling plasma-optical emissive spectrum (IRIS Advantage; Nippon Jarrell-Ash Co., Japan). The Brunauer−Emmett−Teller (BET) surface areas and pore features were measured via nitrogen physisorption (Autosorb-iQ_2-MP; Quantachrome Corp., U.S.A.). Morphology observation was performed using a field-emission transmission electron microscope (JEM 2100F; JEOL Corp., Japan; operated at 200 kV). The diffuse reflectance spectra of the samples were recorded on a UV−visible spectrophotometer (UV-2600; Shimadzu Corp., Japan) with barium sulfate as the reference. Then the absorption spectra were obtained from the reflectance spectra by means of Kubelka−Munk transformations.

Photocatalytic Evaluation. *(1). Isopropyl Alcohol Photodegradation.* A 300 W Xe arc lamp (21 A output current, focused through a 45 × 45 mm shutter window) was employed as the light source for the photocatalytic reaction. A water filter was set between the lamp and the reactor to remove the infrared ray irradiation. The reactor volume was 500 mL; it was equipped with a Pyrex-glass lid as a window. Under such conditions, the wavelength range and intensity of incident light were $\lambda > 300$ nm and 66.9 mW/cm^2, respectively. The light intensities in the photocatalytic reaction were measured using a spectroradiometer (USR-40; Ushio Inc., Japan). The light intensity data were collected from 200 to 800 nm. The 100 mg of sample was spread uniformly in an 8.5 cm^2 plate that was placed in the bottom of the reactor. Then the reactor was pretreated by artificial air [$V(N_2)$:$V(O_2)$ = 4:1] for 5 min to remove adsorbed gaseous impurities. The isopropyl alcohol (IPA) was injected into the reactor to reach saturated adsorption over the samples and, meanwhile, produced a surplus amount of 90−100 μmol in the gas phase. Before irradiation, the reactor was kept in the dark overnight (at least 8 h) until ensuring an adsorption−desorption equilibrium of gaseous reactants on the sample. The concentrations of IPA, acetone, and CO_2 were detected on a gas chromatograph (GC-2014; Shimadzu Corp., Japan) with a flame ionization detector (Details: Porapak Q and TSG-1 columns; temperatures−injector, 120 °C; column, 60 °C; detector, 200 °C).

(2). Photodegradation Mechanism Study. To study the reactive species in the IPA photodegradation, the *t*-butyl alcohol (tBA), ammonium oxalate (AO), and *p*-benzoquinone (pBQ) served as the scavengers for ·OH, h^+, and $\cdot O_2^-$, respectively. For loading the AO and pBQ scavengers on the sample surface, 100 mg of nanoporous $SrTiO_3$ sample was dispersed in 30 mL of ultrapure water in a beaker, and then 5 wt % of scavenger was added. After that, the suspension solution was mixed by 10 min of ultrasonic treatment. Finally, the sample was dried in an oven at 80 °C overnight and then was ready for further photodegradation mechanism study. For introducing the tBA scavenger, the liquid tBA and IPA (molar ratio = 5:95) were mixed well; then, the artificial air was pumped into the mixed organic liquid to bring out the mixed tBA and IPA vapor which was collected into a closed gas bag. In the test of studying the influence of the tBA scavenger, the mixed tBA and IPA gas was injected into the reactor. The evaluation conditions for the photodegradation mechanism study were similar to the above-mentioned common measurement, except that the light intensity was decreased to be 7.4 mW/cm^2 (Xe lamp, 7 A output current, $\lambda > 300$ nm) and the used catalyst was reduced to 50 mg.

ASSOCIATED CONTENT

Supporting Information

Details of synthesis and characterizations, characterizations of SiO_2 nanotemplate, microstructural feature and chemical compositions of nanoporous $SrTiO_3$, calculation of FWHM in XRD pattern, influence of SiO_2 nanotemplate on crystallization, characterizations of commercial nano-$SrTiO_3$, more detailed data of photocatalytic characterizations, characterizations of nanoporous doped $SrTiO_3$, characterizations of nanoporous alkali-metal titanates. This material is available free of charge via the Internet at http://pubs.acs.org.

AUTHOR INFORMATION

Corresponding Authors

*S. Ouyang. E-mail: oysx@tju.edu.cn.

*J. Ye. E-mail: jinhua.ye@nims.go.jp.

Author Contributions

⊥These authors contributed equally. The paper was written through contributions of all authors. All authors have given approval to the final version of the paper.

Notes

The authors declare no competing financial interest.

ACKNOWLEDGMENTS

This work received financial support from the 973Program (No. 2014CB239301), China and the World Premier International Research Center Initiative on Materials Nanoarchitectonics (WPI-MANA), MEXT (Japan).

REFERENCES

(1) Fujishima, A.; Honda, K. Electrochemical Photolysis of Water at a Semiconductor Electrode. *Nature* **1972**, *238*, 37−38.

(2) Malato, S.; Fernandez-Ibanez, P.; Maldonado, M. I.; Blanco, J.; Gernjak, W. Decontamination and Disinfection of Water by Solar Photocatalysis: Recent Overview and Trends. *Catal. Today* **2009**, *147*, 1−59.

(3) Chen, X.; Shen, S.; Guo, L.; Mao, S. S. Semiconductor-based Photocatalytic Hydrogen Generation. *Chem. Rev.* **2010**, *110*, 6503−6570.

(4) Tong, H.; Ouyang, S.; Bi, Y.; Umezawa, N.; Oshikiri, M.; Ye, J. Nano-photocatalytic Materials: Possibilities and Chanllenges. *Adv. Mater.* **2012**, *24*, 229−251.

(5) Roy, S. C.; Varghese, O. K.; Paulose, M.; Grimes, C. A. Toward Solar Fuels: Photocatalytic Conversion of Carbon Dioxide to Hydrocarbons. *ACS Nano* **2010**, *4*, 1259−1278.

(6) Habisreutinger, S. N.; Schmidt-Mende, L.; Stolarczyk, J. K. Photocatalytic Reduction of CO_2 on TiO_2 and Other Semiconductor. *Angew. Chem., Int. Ed.* **2013**, *52*, 2−39.

(7) Kormann, C.; Bahnemann, D. W.; Hoffmann, M. R. Photocatalytic Production of Hydrogen Peroxides and Organic Peroxides in Aqueous Suspensions of Titanium Dioxide, Zinc Oxide, and Desert Sand. *Environ. Sci. Technol.* **1988**, *22*, 798−806.

(8) Wang, C.; Bahnemann, D. W.; Dohrmann, J. K. A Novel Preparation of Iron-Doped TiO_2 Nanoparticles with Enhanced Photocatalytic Activity. *Chem. Commun.* **2000**, *16*, 1539−1540.
(9) Asahi, R.; Morikawa, T.; Ohwaki, T.; Aoki, K.; Taga, Y. Visible-Light Photocatalysis in Nitrogen-Doped Titanium Oxides. *Science* **2001**, *293*, 269−271.
(10) Sakthivel, S.; Kisch, H. Daylight Photocatalysis by Carbon-Modified Titanium Dioxide. *Angew. Chem., Int. Ed.* **2003**, *42*, 4908−4911.
(11) Rehman, S.; Ullah, R.; Butt, A. M.; Gohar, N. D. Strategies of Making TiO_2 and ZnO Visible Light Active. *J. Hazard. Mater.* **2009**, *170*, 560−569.
(12) Scuderi, V.; Impellizzeri, G.; Romano, L.; Scuderi, M.; Brundo, M. V.; Bergum, K.; Zimbone, M.; Sanz, R.; Buccheri, M. A.; Simone, F.; Nicotra, G.; Svensson, B. G.; Grimaldi, M. G.; Privitera, V. An Enhanced Photocatalytic Response of Nanometric TiO_2 Wrapping of Au Nanoparticles for Eco-Friendly Water Applications. *Nanoscale* **2014**, *6*, 11189−11195.
(13) Zou, Z.; Ye, J.; Sayama, K.; Arakawa, H. Direct Splitting of Water under Visible Light Irradiation with an Oxide Semiconductor Photocatalyst. *Nature* **2001**, *414*, 625−627.
(14) Tang, J.; Zou, Z.; Ye, J. Efficient Photocatalytic Decomposition of Organic Contaminants over $CaBi_2O_4$ under Visible-Light Irradiation. *Angew. Chem., Int. Ed.* **2004**, *43*, 4463−4466.
(15) Liu, G.; Wang, L.; Sun, C.; Yan, X.; Wang, X.; Chen, Z.; Smith, S. C.; Cheng, H.; Lu, G. Band-to-Band Visible-Light Photon Excitation and Photoactivity Induced by Homogeneous Nitrogen Doping in Layered Titanates. *Chem. Mater.* **2009**, *21*, 1266−1274.
(16) Mukherji, A.; Seger, B.; Lu, G.; Wang, L. Nitrogen Doped $Sr_2Ta_2O_7$ Coupled with Graphene Sheets as Photocatalysts for Increased Photocatalytic Hydrogen Production. *ACS Nano* **2011**, *5*, 3483−3492.
(17) Ouyang, S.; Ye, J. β-$AgAl_{1-x}Ga_xO_2$ Solid-Solution Photocatalysts: Continuous Modulation of Electronic Structure toward High-Performance Visible-Light Photoactivity. *J. Am. Chem. Soc.* **2011**, *133*, 7757−7763.
(18) Merka, O.; Bahnemann, D. W.; Wark, M. Improved Photocatalytic Hydrogen Production by Structure Optimized Nonstoichiometric $Y_2Ti_2O_7$. *ChemCatChem.* **2012**, *4*, 1819−1827.
(19) Bell, A. T. The Impact of Nanoscience on Heterogeneous Catalysis. *Science* **2003**, *299*, 1688−1691.
(20) Kong, L.; Chen, H.; Hua, W.; Zhang, S.; Chen, J. Mesoporous Bismuth Titanate with Visible-Light Photocatalytic Activity. *Chem. Commun.* **2008**, *40*, 4977−4979.
(21) Fan, X.; Wang, Y.; Chen, X.; Gao, L.; Luo, W.; Yuan, Y.; Li, Z.; Yu, T.; Zhu, J.; Zou, Z. Facile Method To Synthesize Mesoporous Multimetal Oxides ($ATiO_3$, A=Sr, Ba) with Large Specific Surface Areas and Crystalline Pore walls. *Chem. Mater.* **2010**, *22*, 1276−1278.
(22) Fan, X.; Gao, J.; Wang, Y.; Li, Z.; Zou, Z. Effect of Crystal Growth on Mesoporous $Pb_3Nb_4O_{13}$ Formation, and Their Photocatalytic Activity under Visible-Light Irradiation. *J. Mater. Chem.* **2010**, *20*, 2865−2869.
(23) Yan, S.; Ouyang, S.; Gao, J.; Yang, M.; Feng, J.; Fan, X.; Wan, L.; Li, Z.; Ye, J.; Zhou, Y.; Zou, Z. A Room-Temperature Reactive-Template Route to Mesoporous $ZnGa_2O_4$ with Improved Photocatalytic Activity in Reduction of CO_2. *Angew. Chem., Int. Ed.* **2010**, *49*, 6400−6404.
(24) Zhang, N.; Ouyang, S.; Li, P.; Zhang, Y.; Xi, G.; Kako, T.; Ye, J. Ion-Exchange Synthesis of A Micro/Mesoporous Zn_2GeO_4 Photocatalyst at Room Temperature for Photoreduction of CO_2. *Chem. Commun.* **2011**, *47*, 2041−2043.
(25) Tanaka, K.; Capule, M. F. V.; Hisanaga, T. Effect of Crystallinity of TiO_2 on Its Photocatalytic Action. *Chem. Phys. Lett.* **1991**, *187*, 73−76.
(26) Zhang, Q.; Gao, L.; Guo, J. Effects of Calcination on The Photocatalytic Properties of Nanosized TiO_2 Powders Prepared by $TiCl_4$ Hydrolysis. *Appl. Catal., B* **2000**, *26*, 207−215.
(27) Wang, Y.; Xu, H.; Wang, X.; Zhang, X.; Jia, H.; Zhang, L.; Qiu, J. A General Approach to Porous Crystalline TiO_2, $SrTiO_3$, and $BaTiO_3$ Spheres. *J. Phys. Chem. B* **2006**, *110*, 13835−13840.
(28) Ouyang, S.; Tong, H.; Umezawa, N.; Cao, J.; Li, P.; Bi, Y.; Zhang, Y.; Ye, J. Surface-Alkalinization-Induced Enhancement of Photocatalytic H_2 Evolution over $SrTiO_3$-based Photocatalysts. *J. Am. Chem. Soc.* **2012**, *134*, 1974−1977.
(29) Townsend, T. K.; Browning, N. D.; Osterloh, F. E. Overall Photocatalytic Water Splitting with NiO_x−$SrTiO_3$—A Revised Mechanism. *Energy Environ. Sci.* **2012**, *5*, 9543−9550.
(30) Takata, T.; Shinohara, K.; Tanaka, A.; Hara, M.; Kondo, J. N.; Domen, K. A Highly Active Photocatalyst for Overall Water Splitting with a Hydrated Layered Perovskite Structure. *J. Photochem. Photobiol., A* **1997**, *106*, 45−49.
(31) Song, H.; Jiang, H.; Liu, T.; Liu, X.; Meng, G. Preparation And Photocatalytic Activity of Alkali Titanate Nano Materials $A_2Ti_nO_{2n+1}$ (A = Li, Na and K). *Mater. Res. Bull.* **2007**, *42*, 334−344.
(32) Ide, Y.; Nakasato, Y.; Ogawa, M. Molecular Recognitive Photocatalysis Driven by The Selective Adsorption on Layered Titanates. *J. Am. Chem. Soc.* **2010**, *132*, 3601−3604.
(33) Wang, D.; Ye, J.; Kako, T.; Kimura, T. Photophysical and Photocatalytic Properties of $SrTiO_3$ Doped with Cr Cations on Different Sites. *J. Phys. Chem. B* **2006**, *110*, 15824−15830.
(34) Morgado, E.; Marinkovic, B. A.; Jardim, P. M.; de Abreu, M. A. S.; Rocha, M. D. C.; Bargiela, P. Studies on Fe-Modified Nanostructured Trititanates. *Mater. Chem. Phys.* **2011**, *126*, 118−127.
(35) Mao, Y.; Park, T. J.; Wong, S. Synthesis of Classes of Ternary Metal Oxide Nanostructures. *Chem. Commun.* **2005**, *46*, 5721−5735.
(36) Yu, H.; Ouyang, S.; Yan, S.; Li, Z.; Yu, T.; Zou, Z. Sol−Gel Hydrothermal Synthesis of Visible-Light-Driven Cr-Doped $SrTiO_3$ for Efficient Hydrogen Production. *J. Mater. Chem.* **2011**, *21*, 11347−11351.
(37) Liu, J.; Wang, H.; Hou, Y.; Zhu, M.; Yan, H.; Yoshimura, M. Low-Temperature Preparation of $Na_{0.5}Bi_{0.5}TiO_3$ Nanowhiskers by a Sol-Gel-Hydrothermal Method. *Nanotechnology* **2004**, *15*, 777−780.
(38) Xu, H.; Wei, S.; Wang, H.; Zhu, M.; Yu, R.; Yan, H. Preparation of Shape Controlled $SrTiO_3$ Crystallites by Sol-Gel-Hydrothermal Method. *J. Cryst. Growth* **2006**, *292*, 159−164.
(39) Vinu, A. Two-Dimensional Hexagonally-Ordered Mesoporous Carbon Nitrides with Tunable Pore Diameter, Surface Area and Nitrogen Content. *Adv. Funct. Mater.* **2008**, *18*, 816−827.
(40) Xia, Y.; Mokaya, R. Hollow Spheres of Crystalline Porous Metal Oxides: A Generalized Synthesis Route via Nanocasting with Mesoporous Carbon Hollow Shells. *J. Mater. Chem.* **2005**, *15*, 3126−3131.
(41) Chen, C.; Li, X.; Ma, W.; Zhao, J.; Hidaka, H.; Serpone, N. Effect of Transition Metal Ions on The TiO_2-Assisted Photodegradation of Dyes under Visible Irradiation: A Probe for The Interfacial Electron Transfer Process and Reaction Mechanism. *J. Phys. Chem. B* **2002**, *106*, 318−324.
(42) Irmak, S.; Kusvuran, E.; Erbatur, O. Degradation of 4-Chloro-2-Methyphenol in Aqueous Solution by UV Irradaition in The Presence of Titanium Dioxide. *Appl. Catal., B* **2004**, *54*, 85−91.
(43) Jiang, H.; Liu, J.; Cheng, K.; Sun, W.; Lin, J. Enhanced Visible Light Photocatalysis of Bi_2O_3 upon Fluorination. *J. Phys. Chem. C* **2013**, *117*, 20029−20036.
(44) Katsumata, H.; Taniguchi, M.; Kaneco, S.; Suzuki, T. Photocatalytic Degradation of Bisphenol A by Ag_3PO_4 under Visible Light. *Catal. Commun.* **2013**, *34*, 30−34.
(45) Arsac, F.; Bianchi, D.; Chovelon, J. M.; Ferronato, C.; Herrmann, J. M. Experimental Microkinetic Approach of the Photocatalytic Oxidation of Isopropyl Alcohol on TiO_2. Part 1. Surface Elementary Steps Involving Gaseous and Adsorbed C_3H_xO Species. *J. Phys. Chem. A* **2006**, *110*, 4202−4212.
(46) Arsac, F.; Bianchi, D.; Chovelon, J. M.; Ferronato, C.; Herrmann, J. M. Experimental Microkinetic Approach of the Photocatalytic Oxidation of Isopropyl Alcohol on TiO_2. Part 2. From the Surface Elementary Steps to the Rates of Oxidation of the C_3H_xO Species. *J. Phys. Chem. A* **2006**, *110*, 4213−4222.